

# Synthesis, Self-assembly, and Crystal Structure of a Shape-Persistent Polyhedral-Oligosilsesquioxane-Nanoparticle-Tethered Perylene Diimide

Xiangkui Ren,<sup>†,‡</sup> Bin Sun,<sup>†,§</sup> Chi-Chun Tsai,<sup>†</sup> Yingfeng Tu,<sup>†</sup> Siwei Leng,<sup>†</sup> Kaixia Li,<sup>§</sup> Zhuang Kang,<sup>†,§</sup> Ryan M. Van Horn,<sup>†</sup> Xiaopeng Li,<sup>†</sup> Meifang Zhu,<sup>§</sup> Chrys Wesdemiotis,<sup>†</sup> Wen-Bin Zhang,<sup>\*,†</sup> and Stephen Z. D. Cheng<sup>\*,†</sup>

Department of Polymer Science and Department of Chemistry, The University of Akron, Akron, Ohio 44325-3909; Photonics Research Center, The MOE Key Lab of Weak-Light Nonlinear Photonics Materials, and Tianjin Key Lab of Photonics Materials and Technology for Information Science, Nankai University, Tianjin 300071, P. R. China; and State Key Laboratory for Modification of Chemical Fibers and Polymer Materials, College of Materials Science and Engineering, Donghua University, Shanghai 201620, P. R. China

Received: January 6, 2010; Revised Manuscript Received: March 11, 2010

A novel organic–inorganic hybrid with two polyhedral oligosilsesquioxane (POSS) nanoparticles covalently attached to perylene diimide (PDI) via a rigid 1,4-phenylene linkage (POSS-PDI-POSS) was designed and synthesized to examine the effect of bulky and well-defined nanoparticle side chains on the self-assembly behavior of PDI derivatives. The molecules were self-assembled directly by slow evaporation of a cast drop from solution in tetrahydrofuran to give rise to uniform crystalline nanobelts with dimensions typically of 0.2 mm  $\times$  1  $\mu$ m  $\times$  50 nm. The phase behavior and crystal structure of the sample were then elucidated via a combination of different experimental techniques such as differential scanning calorimetry (DSC), wide-angle X-ray diffraction (WAXD), selected area electron diffraction (SAED) in transmission electron microscopy (TEM), polarized light microscopy, and atomic force microscopy. One-dimensional (1D) WAXD and DSC revealed that only one crystalline phase exists. Based on the 2D WAXD fiber pattern obtained from the oriented POSS-PDI-POSS samples, the crystalline structure was determined to be a triclinic unit cell with dimensions of  $a = 6.577$  nm,  $b = 5.213$  nm,  $c = 1.107$  nm,  $\alpha = 93.26^\circ$ ,  $\beta = 94.85^\circ$ , and  $\gamma = 92.73^\circ$ , which was confirmed by SAED experiments on the single crystals with different crystal zone orientations. The detailed molecular conformational analysis indicated that the steric hindrance of the POSS nanoparticles covalently attached to PDI via a rigid 1,4-phenylene linkage makes it difficult to achieve a continuous stacking of PDIs. Instead, the molecules dimerized to maximize the  $\pi$ – $\pi$  interaction. The dimers then became the building blocks and packed themselves into the unit cell. This strong tendency for dimerization was supported by concentration-dependent ultraviolet/visible absorption spectra, fluorescence spectra, and tandem mass spectroscopy with traveling wave ion mobility separation. The combined SAED and TEM results showed that the  $c^*$ -axis of the crystal is along the elongated direction of the single-crystal nanobelt and the normal direction of the  $\pi$ – $\pi$  stacking is along the  $a^*$ -axis. A crystal structure with six dimers as one supramolecular motif in one unit cell was proposed to account for the unusually large unit cell dimensions. The complex structure could be attributed to the longitudinal, transverse, and slightly rotational offsets between the PDIs in the dimers and interdigitated neighboring dimers due probably to both electrostatic interactions and steric demands. The molecular packing scheme in the crystal was simulated using Cerius<sup>2</sup> software, and the resulting diffraction data agreed well with the experimental results. The rationale for such 1D nanostructured morphology formation is also discussed.

## Introduction

Self-assembled, low-dimensional, nanostructured organic semiconductors, such as nanowires and nanobelts, have attracted numerous research interests in the recent decade in an effort to utilize their advantages over their inorganic counterparts, such as low cost, light weight, high flexibility, ease of processing, and virtually unlimited choices of

molecular structures for property optimization, in the construction of molecular electronics.<sup>1–8</sup> It has been well recognized that the supramolecular arrangements of the electrically active molecules over different length scales in these assemblies<sup>9,10</sup> are key to achieve high device performance in various electronic applications such as organic light-emitting diodes,<sup>11,12</sup> photovoltaic cells,<sup>13</sup> field effect transistors,<sup>14–16</sup> and chemical sensors.<sup>17,18</sup> Many functional substituents have been introduced to modify the chemical structure and interplay with the strong  $\pi$ – $\pi$  interaction to aid the supramolecular organization of these molecules.<sup>19</sup> Their effects on the phase behavior, crystal structure, thermal and photophysical properties, and electronic properties have also been studied.<sup>20,21</sup>

\* To whom correspondence should be addressed: E-mail: wz8@uakron.edu (W.-B.Z.); scheng@uakron.edu (S.Z.D.C.). Tel: +1 330 990 9801; (W.-B.Z.); +1 330 972 6931 (S.Z.D.C.). Fax: +1 330 972 8626 (W.-B.Z.); +1 330 972 8626 (S.Z.D.C.).

<sup>†</sup> The University of Akron.

<sup>‡</sup> Nankai University.

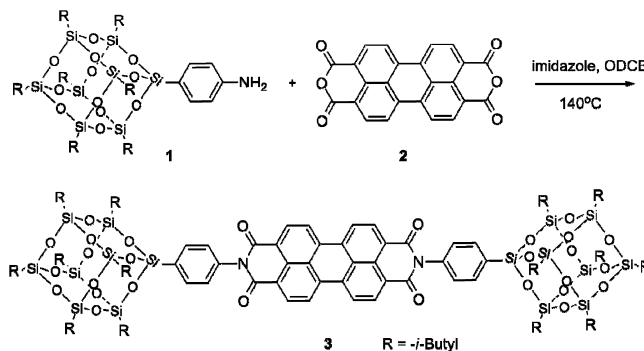
<sup>§</sup> Donghua University.

Among all the  $\pi$ -conjugated building blocks studied in this area, perylene diimides (PDIs) perhaps attract the most attention and have received the widest applications.<sup>22</sup> Unlike most organic semiconductors that are normally p-type in nature, PDIs form a unique robust family of n-type semiconductors with high thermal and photostability.<sup>15,23,24</sup> Moreover, they can be readily obtained and chemically modified for structure–property relationship elucidation and optimization from commercially available starting materials. Various side substituents at the nitrogen atoms in PDIs have been introduced both symmetrically and asymmetrically to tune the self-assembly and the final material structure and properties.<sup>19,21,25–27</sup> An elegant example would be the fabrication of ultralong nanobelts from an asymmetrically substituted PDI with one branched alkyl side chain and one polyoxyethylene chain, as reported by Zang et al.<sup>28</sup> The effect of side chains on self-assembly has been studied,<sup>29</sup> and it has been shown that the structural parameters of PDI derivatives, including interplanar distance, lateral sideway slippage along the short or long axis of the PDI ring, and the in-plane torsion angle between PDIs, are the dominating factors that definitively affect the electronic and optical properties.<sup>30</sup> Small structure differences will induce significant changes in the electronic and optical properties. As a result, despite the many studies reported in the literature, a comprehensive understanding on the structure and molecular packing of crystals and the principles that guide the molecular design of these low-dimensional self-assembly moieties are still lacking. It is interesting and necessary to look at other factors such as the shape and conformation effects that may sometimes play a critical role in determining the crystal structure and formation kinetics. Among all these factors, an intriguing question would be the effect of a bulky and well-defined nanoparticle side chain (or end group) on the self-assembly of  $\pi$ -conjugated systems.

Previous studies in our group have shown that bulky substituents and branched alkyl tails are most effective at modifying phase structures and molecular packings.<sup>31,32</sup> Conventional wisdom has been that the bulkier substituents are more likely to interfere with and disrupt the  $\pi$ – $\pi$  interaction and thus disfavor the ordered structural formation.<sup>3,29</sup> A delicate balance between the side chain and the  $\pi$ – $\pi$  stacking must be achieved for desired assembly.<sup>3</sup> In an extreme case, we ask that if bulky, noncompressible nanoparticles with well-defined sizes are attached to  $\pi$ -conjugated systems such as PDIs, will the molecules still prefer a 1D continuous  $\pi$ – $\pi$  stacking? Can the molecules still be self-assembled into the characteristic 1D nanostructured morphology? What is the role of the overall molecular shape in this self-assembly? To the best of our knowledge, there have been few reports addressing these questions.<sup>20</sup>

Polyhedral oligosilsequioxanes (POSS), regarded loosely as the smallest possible silica nanoparticle with diameter up to 1.5 nm<sup>33</sup> including the side chains at the corners, were chosen as the nanoparticle structural motif because of their well-defined nature and ease in chemical modification. POSS materials have been known for their chemical and thermal robustness and have found wide applications in coating, nanocomposites, electronic devices, and space shuttles.<sup>33,34</sup> There are advantages in incorporating POSS into electroactive conjugated materials: (1) solubility can be significantly enhanced, which facilitates processing; (2) it can impart high thermal and oxidative stability to the material, as already reported;<sup>35</sup> (3) it is possible to functionalize POSS to manipulate their self-assembly and create novel multifunctional materials, which is a significant advantage over other simpler groups; and (4) the highly crystalline packing

### SCHEME 1: Synthesis and Chemical Structure of Compound 3



of POSS cages can sometimes aid the self-assembly in forming ordered structures in the solid state. Nevertheless, there are few reports on the systematic study of the POSS nanoparticles' effect on the self-assembly and ordered packing of  $\pi$ -conjugated materials in the solid state. It is, therefore, chosen as a structural motif to couple with PDI as a model system to examine this effect.

There are basically two ways to link POSS to both nitrogen atoms of PDI: through a rigid linkage or a flexible linkage. The former gives a shape-persistent dumbbell-like molecule, while the latter gives a flexible rattle-drum-like molecule, which also allows us to examine the effect of shape and conformation on self-assembly. Inspired by self-assembly in biological systems, the importance of molecular shape and shape persistence in self-assembly has been gradually recognized in recent years.<sup>36–38</sup> For example, it has been found that the coplanar geometry of a tetracyclic arylene ethynylene macrocycle with a carbonyl-linked alkyl side chain enabled effective 1D self-assembly simply by dispersing a solution into a poor solution or directly by evaporating on a surface while the saddle-shaped tetracycle counterpart requires more strictly controlled assembling conditions.<sup>39</sup> Meanwhile, if a flexible linkage is used, the nanoparticle and the  $\pi$ -conjugated plane are decoupled in this case, and the nanoparticle will exhibit less influence on the self-assembly of the  $\pi$ -conjugated planes.<sup>20</sup> Therefore, we focus on the POSS-PDI conjugate with rigid linkages.

In this publication, we report the molecular design, synthesis, and self-assembly of a novel shape-persistent POSS-PDI-POSS conjugate molecule **3** (Scheme 1). The POSS nanoparticles are covalently attached to PDI via a rigid 1,4-phenylene linkage. The shape of the molecule is thus well-defined due to limited conformational freedom. Surprisingly, it has been found that **3** could be self-assembled into uniform, ultralong crystalline nanobelts with dimensions typically of 0.2 mm  $\times$  1  $\mu$ m  $\times$  50 nm simply by slow evaporation of a solution cast drop from tetrahydrofuran (THF). The crystal structure and phase behavior were then determined using differential scanning calorimetry (DSC), polarized light microscopy (PLM), one- and two-dimensional (1D and 2D) wide-angle X-ray diffraction (WAXD), and selected area electron diffraction (SAED). The molecular packing scheme of the molecules in the crystalline nanobelts has been simulated via computer calculation, and the results have agreed well with experimental observations. We have also provided the reason for the formation of such 1D nanobelt morphology.

### Experimental Section

**Materials.** *p*-Aminophenylisobutyl POSS (**1**, Hybrid Plastics, AM0292,  $\geq 97\%$ ), perylene-3,4,9,10-tetracarboxylic dianhydride

(**2**, Aldrich,  $\geq 98.0\%$ ), imidazole (ACS reagent, Aldrich,  $\geq 99\%$ ), 1,2-dichlorobenzene (ODCB, Aldrich, anhydrous,  $99\%$ ), chloroform (ACS reagent, Aldrich,  $\geq 99.8\%$ ), and tetrahydrofuran (THF, Aldrich, anhydrous and inhibitor-free,  $\geq 99.9\%$ ) were used as received. Silver-plated aluminum foil used for the oriented crystal growth was put into 10% nitric acid for 10 s, washed with deionized water and acetone and then dried under vacuum.

**Synthesis of 3.** The compound was prepared according to Scheme 1 using the method described in previous reports.<sup>29,40</sup> *p*-Aminophenylisobutyl POSS (**1**, 0.50 g, 0.55 mmol), perylene-3,4,9,10-tetracarboxylic dianhydride (**2**, 0.072 g, 0.18 mmol), imidazole (2.0 g), and 4 mL of *o*-dichlorobenzene (ODCB) were placed in a round-bottom flask fitted with a reflux condenser. Under an argon atmosphere, the mixture was heated in an oil bath at 140 °C with vigorous stirring for 6 h. It was then cooled and dispersed in 50 mL of ethanol and 50 mL of 2N HCl overnight. The mixture was extracted with 200 mL of chloroform two times. The combined organic phase was washed with 5% NaHCO<sub>3</sub> aqueous solution until neutral and then with brine. After drying over anhydrous sodium sulfate, it was concentrated, loaded into a silica gel column, and eluted with hexane/ethyl acetate (*v/v* = 10:1). The colored fraction was collected, which was a mixture of the desired product and unreacted **1**. It was further purified by dissolving in chloroform and adding methanol to induce the precipitation of **3** by slow diffusion. The product was collected by filtration as a dark red solid (0.185 g). Yield: 47%. <sup>1</sup>H NMR (CDCl<sub>3</sub>, 500 MHz, ppm,  $\delta$ ): 8.79 (d, *J* = 8.1 Hz, 4 H), 8.72 (d, *J* = 8.1 Hz, 4 H), 7.88 (d, *J* = 8.1 Hz, 4 H), 7.38 (d, *J* = 8.3 Hz, 4 H), 1.92 (m, 14 H), 0.99 (dd, *J* = 6.6, 3.2 Hz, 84 H), 0.67 (m, 28 H). <sup>13</sup>C NMR (CDCl<sub>3</sub>, 125 MHz, ppm,  $\delta$ ): 163.46, 136.84, 135.24, 135.05, 132.98, 131.91, 129.89, 127.78, 126.78, 123.56, 123.40, 25.74, 25.72, 23.90, 22.55, 22.48. FT-IR (KBr)  $\nu$  (cm<sup>-1</sup>): 2956, 2926, 2871, 1712 (C=O), 1673, 1594, 1504, 1464, 1385 (C–N), 1352, 1229, 1105 (Si–O), 838, 743, 691, 483, 428. MS (MALDI-TOF analysis, *m/z*): Calcd for C<sub>92</sub>H<sub>142</sub>N<sub>2</sub>NaO<sub>28</sub>Si<sub>16</sub> (M + Na<sup>+</sup>): 2193.60; Found: 2193.58 (M + Na<sup>+</sup>, 100%).

**Sample Preparation.** Single-crystalline nanobelts were prepared by solution-casting a dilute 0.01 (w/v) % THF solution on carbon-coated mica surfaces under slow evaporation in a THF-saturated atmosphere. After crystallization, the single crystals were removed from the mica surface and collected on copper grids for transmission electron microscopy (TEM). The procedure was repeated on different substrates, such as carbon-coated glass and silver-plated aluminum foil, to prepare samples for 1D/2D WAXD, polarized light microscopy (PLM), and atomic force microscopy (AFM). For 2D WAXD experiments, oriented crystalline samples were needed to obtain fiber patterns. It could be achieved via surface-supported self-assembly by submerging one end of a silver-plated aluminum foil in the 0.3 (w/v) % THF solution and allowing slow evaporation to use the crystalline silver substrate as a template for orientation. The oriented beltlike crystals were grown along the surface of the silver-plated aluminum foil for 3 days during which all the solvent evaporated. For the DSC experiment, about 4 mg of sample was used, and the pan weights were kept constant to the precision of  $\pm 0.001$  mg.

**Equipment and Experiments.** All <sup>1</sup>H and <sup>13</sup>C NMR spectra were acquired in CDCl<sub>3</sub> (Aldrich, 99.8% D) using a Varian 500 NMR spectrometer. The <sup>1</sup>H NMR spectra were referenced to the residual proton impurities in the CDCl<sub>3</sub> at  $\delta$  7.27 ppm. <sup>13</sup>C NMR spectra were referenced to <sup>13</sup>CDCl<sub>3</sub> at  $\delta$  77.00 ppm. Infrared spectra were recorded on an Excalibur Series FT-IR

spectrometer (DIGILAB, Randolph, MA) by casting polymer films on KBr plates from dilute THF solutions. UV–vis spectra were recorded on an HP 8453 UV–vis spectrometer system.

Photoluminescence (PL) spectra and the corresponding excitation spectra were measured in the reflection geometry by positioning the samples at an angle of 45° to the incident radiation on a Jobin Yvon Fluorolog-3-Tau steady-state fluorescence spectrophotometer. A Xe lamp was utilized as the excitation light source. The excitation wavelength was at 497 nm. All the measurements were carried out at room temperature in ambient air. The analysis range was 200–800 nm with a resolution of 1 nm. The quantum yield of fluorescence of the sample in dilute CHCl<sub>3</sub> solution was measured using Rhodamine 6G as a standard and calculated using eq 1:

$$\Phi_{\text{unk}} = \Phi_{\text{std}} \times \left( \frac{I_{\text{unk}}}{I_{\text{std}}} \right) \times \left( \frac{A_{\text{std}}}{A_{\text{unk}}} \right) \times \left( \frac{n_{\text{unk}}}{n_{\text{std}}} \right)^2 \quad (1)$$

where  $\Phi_{\text{unk}}$  is the fluorescence quantum yield of the sample,  $\Phi_{\text{std}}$  is the fluorescence quantum yield of the standard,  $I_{\text{unk}}$  and  $I_{\text{std}}$  are the integrated emission intensities of the sample and the standard, respectively,  $A_{\text{unk}}$  and  $A_{\text{std}}$  are the absorbance of the sample and the standard at the excitation wavelength, respectively, and  $n_{\text{unk}}$  and  $n_{\text{std}}$  are the refractive indexes of the corresponding solution.

The thermal properties of **3** were characterized by utilizing a Perkin-Elmer PYRIS Diamond DSC with an Intracooler 2P apparatus. The temperature and heat flow scales were calibrated at different heating and cooling rates (1–40 °C/min) using standard materials. 1D WAXD powder pattern was taken at room temperature with a Rigaku MultiFlex 2 kW tube-anode X-ray (Cu K $\alpha$  radiation) generator coupled to a diffractometer. The samples were scanned at a 1°/min scanning rate. The peak positions were calibrated using silicon powder in the high-angle region ( $>15^\circ$ ) and silver behenate in the low-angle region ( $<15^\circ$ ). Background scattering was subtracted from the sample pattern. For 2D WAXD pattern, a Rigaku 18 kW rotating anode X-ray generator attached to an R-AXIS-IV image plate system was used. The exposure time to obtain high-quality WAXD pattern was 30 min. The same standards were used to calibrate the  $2\theta$  angles. The crystal unit cell was determined by constructing reciprocal lattices using the software we developed. Density measurement was carried out at room temperature using a Gay-Lussac type specific gravity bottle (10 mL). An aqueous solution of potassium iodide was used to find the density of crystallized samples.

TEM experiments were carried out with a Philips Tecnai 12 using an accelerating voltage of 120 kV. Selected area electron diffraction (SAED) patterns with different crystal orientations were obtained by using a tilting stage to determine the crystal structure parameters. The *d*-spacings were calibrated using a TiCl standard. The tilting angle was defined as positive if the tilting direction was clockwise and negative for counterclockwise. PLM observation was performed on an Olympus (HB-2) microscope under reflection mode. AFM (Digital Instruments Nanoscope IIIA) was used to examine the crystals grown on the mica substrate with a 100  $\mu\text{m}$  scanner under the tapping mode. The cantilever force was light enough to avoid any damage to the sample, yet strong enough so that the surface features could be accurately explored. The scanning rate was 1 Hz for low-magnification images at a resolution of  $512 \times 512$  pixels per image.

Electrospray ionization (ESI) mass spectra were obtained on a Waters Synapt HDMS quadrupole/time-of-flight (Q/ToF)



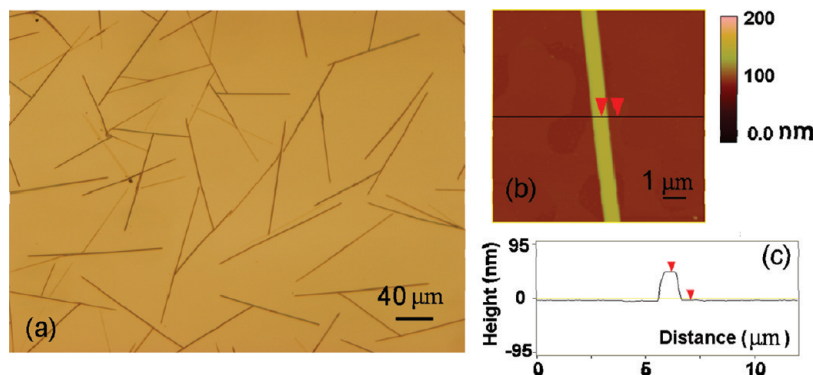


**Figure 1.** (a) PLM images of single-crystalline nanobelts of **3** prepared by slow evaporation from a 0.01% THF solution on a carbon-coated mica surface; (b) AFM image of single-crystalline nanobelts of **3**; and (c) a line-scan profile clearly reveals the flat top of the crystal with a thickness of 50 nm.

tandem mass spectrometer equipped with traveling wave ion mobility (TWIM) separation.<sup>41</sup> The TWIM device is located between the Q/ToF mass analyzers and consists of three parts, a trap cell, an ion mobility (IM) cell, and a transfer cell. The trap and transfer cells can be used for conventional tandem mass spectrometry experiments via collisionally activated dissociation (CAD). The ion mobility cell is used in IM separations. The following parameters were used in the TWIM-MS experiments: ESI capillary voltage, 3.5 kV; sample cone voltage, 35 V; extraction cone voltage, 3.2 V; desolvation gas flow, 800 L/h ( $N_2$ ); trap collision energy (CE), 6 eV; transfer CE, 4 eV; trap gas flow, 1.5 mL/min (Ar); IM gas flow, 22.7 mL/min ( $N_2$ ); sample flow rate, 10  $\mu$ L/min; source temperature, 30  $^{\circ}$ C; desolvation temperature, 40  $^{\circ}$ C; IM traveling wave velocity, 380 m/s; and IM traveling wave height, 15 V. In the tandem mass spectrometry (MS/MS) experiments, argon was used as the collision gas and the trap CE was varied from 6 to 55 eV to cause fragmentation. The sprayed solution was prepared by dissolving  $\sim$ 1 mg of sample in 1 mL of a MeOH/THF (v/v = 1:3) mixture and adding 5  $\mu$ L of 10 mg/mL NaTFA in THF as the cationizing agent.

**Molecular Modeling.** Molecular modeling and analysis of the diffraction patterns were performed using the Cerius<sup>2</sup> package of Accelrys. The lowest energy conformation of **3** was chosen as the starting conformation. Basic unit cell parameters determined by crystallographic experimental data from 2D WAXD and SAED experiments were used to build the crystal unit cell. The positions of atoms in this unit cell were judged by comparing their calculated diffraction patterns with those of experiments.

## Results and Discussion

**Molecular Design and Synthesis.** Perylene diimides have been widely used as building blocks for self-assembly into low-dimensional organic semiconductor materials (liquid crystals,<sup>19,26</sup> nanowires,<sup>25,42</sup> nanobelts,<sup>43</sup> etc.) because of their facile synthetic availability and strong  $\pi$ - $\pi$  interaction.<sup>22</sup> To investigate the effect of a nanoparticle side chains, the POSS nanoparticle should be covalently attached to PDIs via a spacer or linkage. In our study, a rigid 1,4-phenylene linkage was chosen so that the POSS and PDI are closely coupled together to allow the least conformational freedom. Such a stiff, shape-persistent dumbbell with a  $\pi$ -conjugated plane center is expected to exhibit interesting self-assembly behavior. Therefore, in this work, we focus on the shape-persistent conjugate molecule **3**.

Using the standard condensation method developed by Langhals,<sup>40</sup> the target molecule **3** was conveniently synthesized

in one step from commercially available starting materials **1** and **2**. The yield of 47% was acceptable given that the reaction conditions were not optimized. It is possible that mono-POSS end-capped products (POSS-PDI) might form and were not converted further to **3**. Such intermediates have anhydride bonds which hydrolyze during the workup procedure and thus possess high polarity, making them hard to elute from the column. Therefore, the desired product **3** could be readily separated from them by chromatography. After further purification by slow diffusion to remove the unreacted amine, the product was obtained as a red solid. In contrast to most PDI derivatives that have very limited solubility, compound **3** shows high solubility in common organic solvents such as hexane, THF,  $CH_2Cl_2$ , and chloroform, which facilitates the processing and self-assembling process. The unusual solubility is a result of the POSS nanoparticles substituted with many isobutyl groups and the steric demand that reduces the strong  $\pi$ - $\pi$  interaction.

Compound **3** has been fully characterized by  $^1H$  NMR (Figure S1 (Supporting Information)),  $^{13}C$  NMR (Figures S2 and S3 (Supporting Information)), FT-IR, UV-vis (Figure 6a), fluorescence (Figure 6b), and MALDI-TOF mass spectrometry to unambiguously establish its chemical identity. Perylene diimides are known to have very high quantum yields, and a quantum yield of unity compared with the standard (Rhodamine 6G) in good solvent is not uncommon for PDI derivatives.<sup>29</sup>

**Crystalline Nanobelt Formation and Crystal Structure Determination.** Normally, the attachment of a bulky side chain would significantly affect the  $\pi$ - $\pi$  stacking and disfavor self-assembly. To our surprise, simply by evaporation of a dilute solution in THF on a carbon-coated mica surface, single crystals can be grown that resemble the shape of a nanobelt. Figure 1a shows the single crystals in the shape of nanobelts observed under reflection mode of PLM. An individual nanobelt-shaped single crystal can be clearly seen in the AFM image of Figure 1b. The line-scan profile over the transverse direction of the single crystal demonstrates a flat top surface and a typical thickness of  $\sim$ 50 nm (Figure 1c). The width of the nanobelt is around 1  $\mu$ m (Figure 1b,c), while the length of the single crystals can be as long as several hundred micrometers (Figure 1a).

To determine its phase behavior and crystal structure, a DSC cooling and subsequent heating scan of **3** at a scanning rate of 10  $^{\circ}$ C/min between room temperature and 250  $^{\circ}$ C was first obtained. The thermogram shows no phase transition during the temperature range studied. On the other hand, 1D WAXD pattern as shown in Figure 2 exhibits sharp diffraction peaks in both low and high  $2\theta$ -angle regions, indicating that the nanobelts of **3** do possess a crystalline-ordered structure. Furthermore,

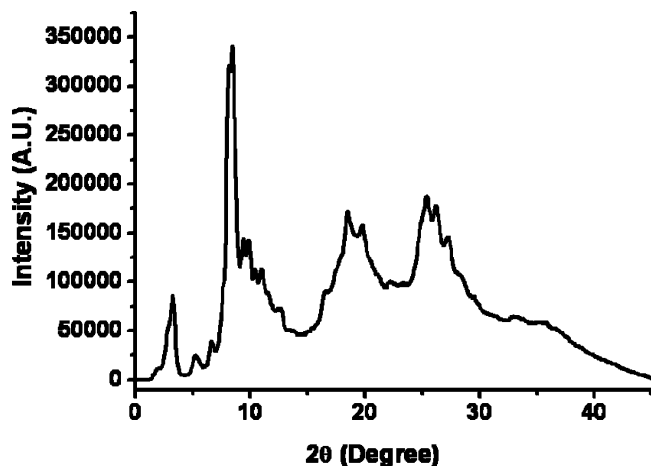


Figure 2. 1D WAXD pattern of **3**.

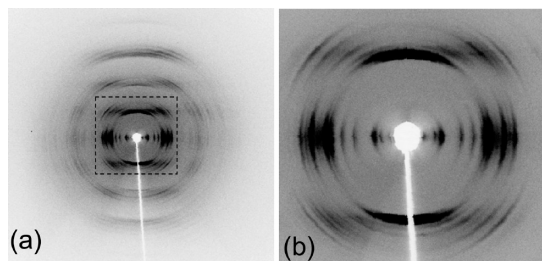


Figure 3. 2D WAXD fiber pattern of **3**: (a) overview; (b) a zoom-in view at the center part of the diffraction pattern.

since there is no thermal transition observed in DSC experiments, we conclude that the nanobelts of **3** are crystalline and that there is only one phase in this temperature region. The 1D WAXD powder pattern lacks lattice dimensionality of the crystal structure, and it is not sufficient for a complete structure determination.

To precisely determine the crystal structure of **3**, a 2D WAXD fiber pattern from oriented crystals is required. The oriented samples could be obtained by surface-supported self-assembly as described in the Experimental Section. Figure 3 shows a 2D WAXD pattern obtained from the oriented crystals. The  $d$ -spacings of these diffraction arcs correspond well to those in the 1D WAXD pattern shown in Figure 2. According to the principles of the reciprocal lattice, the  $a^*$ - and  $b^*$ -axes are tentatively assumed to be on the equator; namely, the  $(hk0)$  diffractions are thus on the equator. Furthermore, if the  $c^*$ -axis is along the meridian, the crystal structure must be either orthorhombic or monoclinic. However, if the  $c^*$ -axis is off the meridian, it depends upon the relationship between  $a^*$ - and  $b^*$ -axes. When the angle  $\gamma^*$  between these two reciprocal axes is not  $90^\circ$ , a triclinic lattice has been formed. Following the standard procedure of determining the crystal lattice,<sup>44–47</sup> a triangle of the  $(hk0)$  diffractions on the equator direction can be constructed, and all of the  $(hk0)$  diffractions can be indexed based on the triangle. On the other hand, we observed that the  $c^*$ -axis is off the meridian, and the diffractions show third-order peaks. The  $d$ -spacing ratios of these diffractions are 1:2:3, indicating a layered structure along this direction in the crystals. The first diffraction arc has been assigned as the  $(001)$  diffraction with the smallest diffraction angle ( $2\theta = 8.03^\circ$ ). This corresponds to a  $d$ -spacing of 1.101 nm, which is slightly larger than the width of the molecule **3** ( $\sim 1$  nm).<sup>19</sup> Therefore, this layer spacing must be attributed to the edge-to-edge organization of molecules. Using the refinement procedure developed in our laboratory,<sup>44–47</sup> the unit cell of the crystal was finally determined

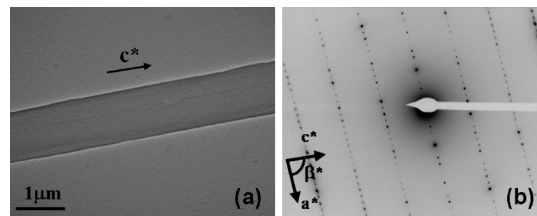
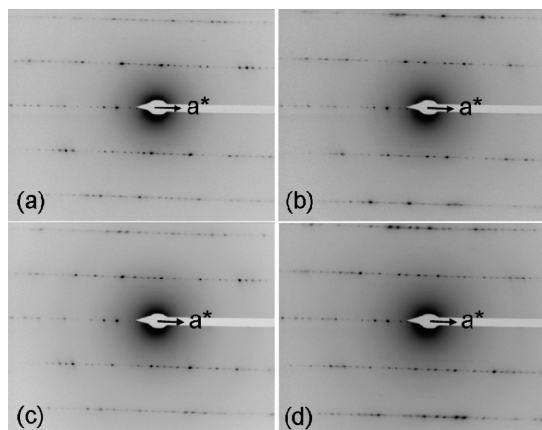


Figure 4. (a) TEM bright field image of the single-crystal nanobelt morphology; (b) SAED pattern of the  $[010]$  zone without tilting obtained from the crystal.

to be triclinic with dimensions of  $a = 6.577$  nm,  $b = 5.213$  nm,  $c = 1.107$  nm,  $\alpha = 93.26^\circ$ ,  $\beta = 94.85^\circ$ , and  $\gamma = 92.73^\circ$  containing 12 molecules as a motif in the crystal. Such a large unit cell dimension is quite remarkable and implies a complex molecular packing scheme and motif symmetry in the unit cell, probably due to longitudinal, transverse, and rotational offsets among the PDIs in the crystal. The experimental and calculated diffraction angles ( $2\theta$ ) and  $d$ -spacing values of the crystal lattice are listed in Table S1 (see Supporting Information). It should be noted that the  $d$ -spacing of  $(100)$  at 6.577 nm is not directly detected in our 2D WAXD because it is at a low angle of  $1.35^\circ$  that is out of our 2D WAXD detecting range. It is later confirmed by the SAED experiments in TEM. The calculated crystallographic density is  $1.15$  g/cm<sup>3</sup> with 12 molecules in each unit cell, which is in good agreement with the experimental result of  $1.14$  g/cm<sup>3</sup>.

Figure 4a shows part of the single-crystal morphology observed in TEM, and Figure 4b is the corresponding SAED pattern. As shown in this figure, the strong  $(020)$  diffraction found in the 2D WAXD pattern on the equator (Figure 3) cannot be observed in this SAED pattern. The reciprocal angle between the two reciprocal axes is  $85^\circ$ , which is consistent with the  $(180^\circ - \beta)$  angle calculated from the 2D WAXD experiment. Therefore, this is the  $\beta^*$  angle, and the SAED pattern in Figure 4b must be the  $[010]$  zone ED pattern of this single crystal. Given the single-crystal morphology in Figure 4a, it can be concluded that the  $c^*$ -axis must be parallel to the elongated direction of the single crystal. Along the  $a^*$ -axis in the SAED pattern of Figure 4b, there are 28 diffraction spots and their  $d$ -spacing values follow integral ratios with respect to each other. The triclinic unit cell is primitive and there are no extinction rules for all the diffractions, so that the observed diffraction spots are the  $(200)$ ,  $(300)$ ,  $(400)$ ,  $(500)$ ,  $(600)$ , ... and up to the  $(1400)$  diffractions with a  $d$ -spacing of 3.272 nm for the  $(200)$  diffraction. The strong intensity of the  $(600)$  diffraction spot probably indicates a highly ordered substructure within the unit cell. Considering the characteristics of  $\pi$ – $\pi$  interaction between PDI cores, the  $(600)$  diffraction spot should come from layered molecules packing along the plane normal to the PDI. Along the  $c^*$ -axis in the SAED pattern, five layers of diffraction spots can be detected. The spot corresponding to the smallest angle on the first layer diffraction can be assigned as the  $(001)$  diffraction with a  $d$ -spacing of 1.101 nm. Therefore, the  $ac$ -plane of the 2D unit cell dimensions ( $a = 6.577$  nm,  $c = 1.107$  nm, and  $\beta = 94.85^\circ$ ) are found to agree well with the structure determined utilizing the 2D WAXD results (Figure 3).

Further proof of the crystal structure was obtained from a series of SAED experiments on tilted samples. Figure 5a shows an SAED pattern that was obtained by tilting the sample  $12^\circ$  around the  $a^*$ -axis of the  $[010]$  zone ED pattern (Figure 4b). On the zero diffraction layer along the  $a^*$ -axis, the diffraction pattern and the intensity ratios are identical to those shown in Figure 4b, since the tilting is along the  $a^*$ -axis. However, on



**Figure 5.** SAED patterns from the [011] zone (a), [012] zone (b), [01 $\bar{1}$ ] zone (c), and [01 $\bar{2}$ ] zone (d) at room temperature. The patterns of (a), (b), (c), and (d) were obtained by tilting the sample by 12°, 23°, -11°, and -21° from [010] zone around  $a^*$ -axis, respectively.

the first and second diffraction layers parallel to the  $a^*$ -axis, the diffraction pattern changed, which is direct evidence that this is the ED pattern from a different diffraction zone. These diffraction spots on the first and second diffraction layers parallel to the  $a^*$ -axis have the  $d$ -spacings and angles in good agreements with those calculated utilizing the [011] zone pattern based on the unit cell structure deduced from the 2D WAXD experiments. Therefore, the ED pattern in Figure 5a is taken along the [011] zone. Similarly, the [012] zone ED pattern can be obtained by a 23° tilting of the sample (Figure 5b), while the [01 $\bar{1}$ ] (Figure 5c) and the [01 $\bar{2}$ ] zone (Figure 5d) ED patterns can be obtained by -11° and -21° tilting around the  $a^*$ -axis, respectively. On the basis of these SAED experimental results, the crystallographic parameters of the unit cell determined by WAXD results were confirmed.

For a triclinic unit cell, it is interesting that the ED patterns from the [011] zone (Figure 5a) and [01 $\bar{1}$ ] zone (Figure 5c) are similar to each other and the required tilting angles from [010] zone around the  $a^*$ -axis to achieve these ED patterns are also close. The observation is the same in the cases of the ED patterns along the [012] zone (Figure 5b) and [01 $\bar{2}$ ] zone (Figure 5d). The reason is that the  $\alpha$ ,  $\beta$ , and  $\gamma$  angles of this triclinic unit cell are close to 90° so that the unit cell is not too far deviated from an orthorhombic lattice. We speculate that the triclinic lattice may result from a distorted orthorhombic lattice due to the longitudinal, transverse, and rotational offsets among the PDI  $\pi$ -stacks in order to accommodate the rigid, bulky nanoparticle side chain to minimize free energy. Simulation was used

to gain insight into the solid-state packing of these shape-persistent molecules and account for the tendency of such molecules to form a nanostructured morphology.

#### Crystallographic Simulation of Molecular Packing Scheme.

The first question in building up the molecular packing scheme is to determine the dominant force that guides the molecular packing configurations. Will the PDI in **3** still aggregate with strong  $\pi$ - $\pi$  interaction despite the steric hindrance of the POSS? In order to understand this, concentration-dependent UV/vis spectra and fluorescence spectra of **3** in a mixed solvent of chloroform/methanol ( $v/v = 1:2$ ) were measured and are shown in Figure 6. Chloroform is a good solvent for **3**, while methanol is a poor solvent for **3**. The presence of methanol induced the aggregation in solution. Pronounced changes in both absorption and emission spectra upon increasing concentration were observed. At low concentrations, **3** exhibited typical monomeric  $\pi$ - $\pi$  transition band with three resolved absorption peaks at 528, 491, and 460 nm. Upon increasing concentration, the apparent absorption coefficients of these monomeric absorption peaks decrease gradually with a slightly blue-shifted peak position (ca. 1 nm), and the absorption became broadened and less structured. Meanwhile, a new broad bathochromically shifted band grows at  $\sim 585$  nm (Figure 6a), which is a typical sign of an effective  $\pi$ - $\pi$  interaction with the face-to-face configuration.<sup>29</sup> The formation of cofacial aggregation species is also supported by concentration-dependent fluorescence spectra. The strong  $\pi$ - $\pi$  electronic coupling leads to the significant quenching of the molecular fluorescence upon increasing concentration (Figure 6b). These spectral features are very similar to that for the formation of H-aggregates of PDI derivatives,<sup>30</sup> but the absence of a significantly hypsochromically shifted peak suggests that its packing behavior must be different from the H-aggregates that normally consist of continuously stacked  $\pi$ -planes. Therefore, the spectral change as shown in Figure 6a,b may be explained by the formation of dimeric species that could be representative of atypical H-aggregates which are not continuously packed along the normal direction of the  $\pi$ -planes.

The strong tendency for **3** to form dimers is also observed by tandem mass spectrometry coupled with traveling wave ion mobility (TWIM) separation, which is an experimental technique allowing us to detect supramolecular aggregates with size resolution.<sup>41,48-50</sup> The molecules or supramolecular aggregates were first ionized, and conventional tandem mass spectrometry was applied to destroy the specific aggregate via collisionally activated disassociation (CAD). The ions were then subjected to ion mobility separation by their mass-to-charge ratios and

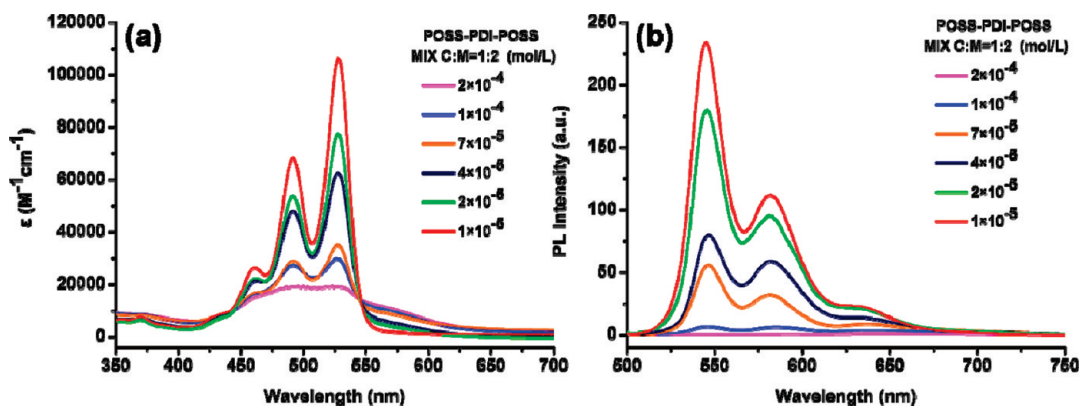


**Figure 6.** Concentration-dependent (a) UV-vis absorption spectra and (b) fluorescence spectra (excitation at 497 nm) of POSS-PDI-POSS **3** in chloroform/methanol ( $v/v = 1:2$ ) mixed solvent ( $1 \times 10^{-5}$  to  $2 \times 10^{-4}$  M).



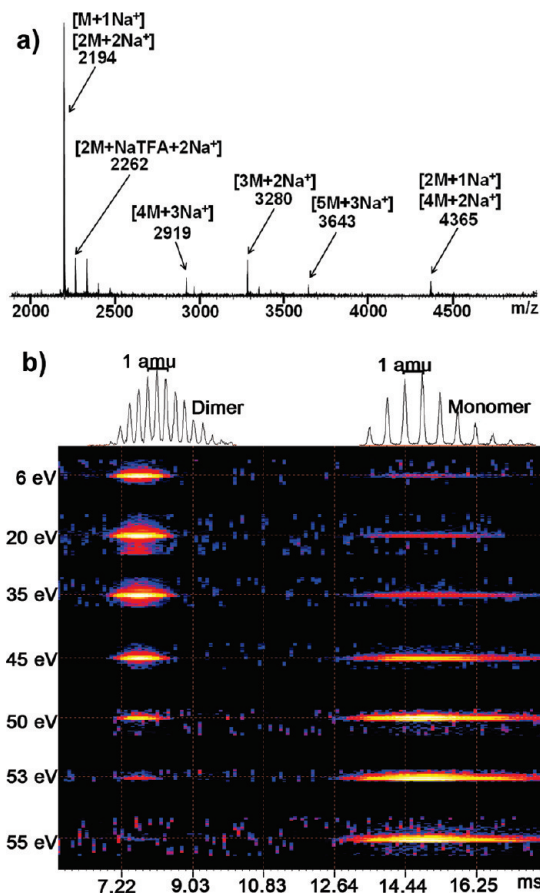


**Figure 7.** ESI mass spectrum of POSS-PDI-POSS acquired on the Waters Synapt quadrupole/time-of-flight (Q/ToF) mass spectrometer. (a) Full mass spectrum of POSS-PDI-POSS (M) using NaTFA for cationization. (b) Two-dimensional ESI-TWIM-MS plot for  $m/z$  2194. Two species, monomer and dimer, were observed at 14.80 and 7.58 ms, respectively. The brightness of the color represents the intensity of the peak. Precursor ions at  $m/z$  2194 were isolated by the Q for subsequent gradient tandem mass spectrometry in a trap cell at collision energies ranging from 6 to 55 eV.

sizes. In the full mass spectrum of **3** in Figure 7a, monomer as well as aggregates of dimer, trimer, tetramer, and up to pentamer with sodium ions were observed, as were NaTFA adducts. The peak with the strongest intensity was the monomer/dimer peak at  $m/z$  2194. With ion mobility separation,  $[2M + 2Na^+]$  was found to be the dominant species for the ions at  $m/z$  2194, while  $[M + Na^+]$  was only detected with trace abundance (Figure 7b, 6 eV). Are the dimers merely aggregated clusters of two monomeric molecules without specific interaction, or are the dimers a result of strong  $\pi$ - $\pi$  interaction? To answer this question, tandem mass spectrometry was used in the trap cell to break the aggregation in the dimeric species. With applied collision CAD energy from 6 to 55 eV, the signal of  $[2M + 2Na^+]$  was decreased and almost disappeared at 53 eV, while the signal of  $[M + Na^+]$  increased due to the dissociation of dimeric species. The results indicated that the dimer was not just the cluster of two  $[M + Na^+]$  that would easily dissociate at low collision CAD energy. Instead, it results from strong  $\pi$ - $\pi$  interaction that could survive energies as high as 53 eV.

To maximize the  $\pi$ - $\pi$  interaction, two PDI planes have to be face to face. The steric repulsion between the rigid and bulky POSS nanoparticles in this case renders a slight bending of the POSS away from the center of the plane and a small offset between the PDI planes. This type of arrangement makes it very difficult for further  $\pi$ - $\pi$  stacking beyond the dimer. Therefore,

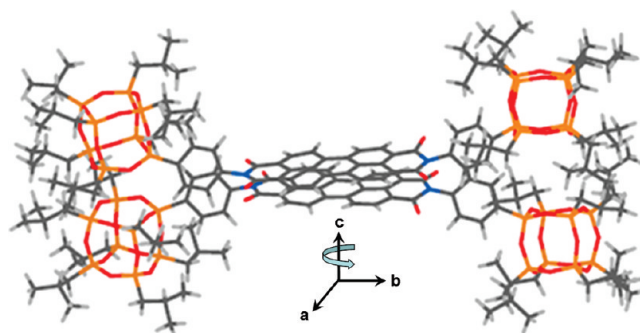


**Figure 8.** Schematic illustration of the direction of (a) transverse displacement, (b) longitudinal displacement, and (c) rotational axis for the PDI dimer.

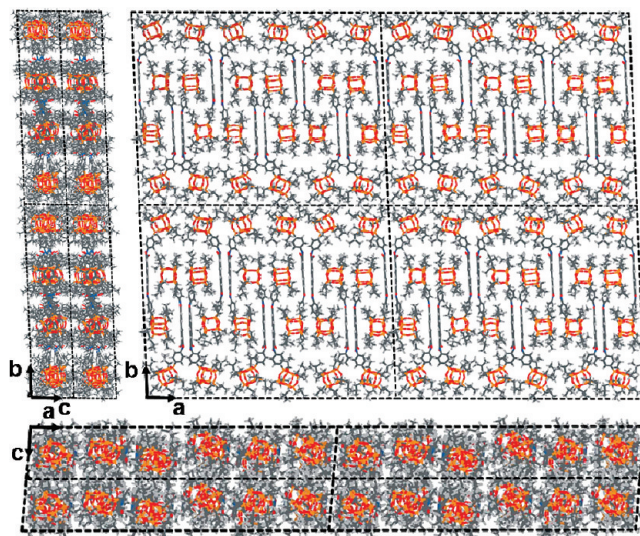


**Figure 9.** Molecular packing in the crystal lattice on three different planes. Upper left,  $bc$ -plane; upper right,  $ab$ -plane; bottom,  $ac$ -plane. Each projection contains 4 unit cells along the projection plane. The orange-red cubes represent POSS cages.

to ensure the close packing in the crystals, it seems very plausible that **3** will form dimers as building blocks to pack in the crystalline lattice.

Based on these assumptions, a primitive molecular packing scheme can be constructed utilizing the Cerius<sup>2</sup> software package. The  $\pi$ - $\pi$  stacked PDI dimers exhibiting the face-to-face geometry with  $\pi$ - $\pi$  plane distance ranging from 0.334 to 0.355 nm are used as motifs.<sup>51</sup> However, this packing scheme construction leads to an orthorhombic or monoclinic unit cell with  $\beta = \gamma = 90^\circ$ . Therefore, the triclinic lattice obtained via experimental data must result from the distortion of the PDI dimers relative to each other.<sup>22,30</sup> A model of the dimer of **3** and the directions for adjustments of relative positions of **3** in the dimer are as shown in Figure 8. First, in each dimer the relative positions of the PDIs can be adjusted along the long axis of the PDI plane (longitudinal displacement). Second, a transverse offset between PDI dimers is allowed (transverse displacement). Third, a rotational offset is introduced. The optimal adjustments are then taken based on the best fit to the results of 2D WAXD and SAED experiments in TEM (Figures 4b and 5a-d).

Figure 9 presents the molecular packing simulation results that generated the diffraction patterns showing the best fit with the experimental observations. In the lattice, the dimers are interdigitated with each other to fill in the space. The  $\pi$ -planes of the dimers are parallel to the  $b$ -axis. The  $b$ -axis (5.213 nm)

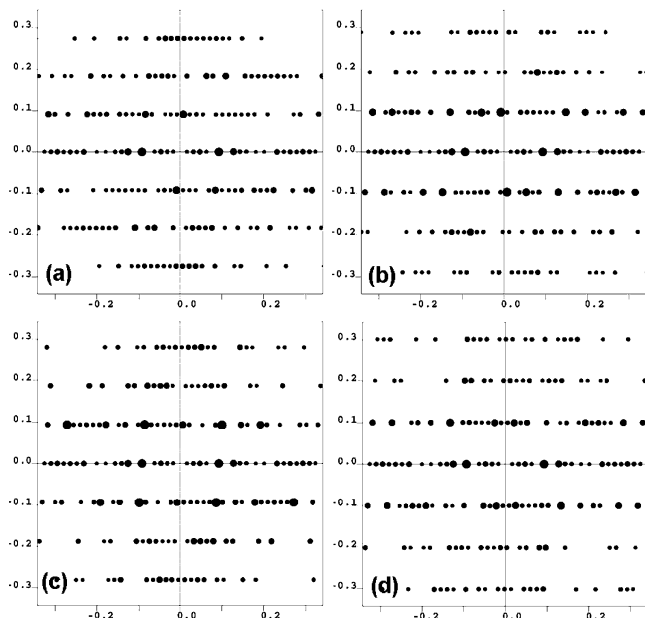


**Figure 10.** Computer-calculated SAED patterns from the [011] zone (a), [012] zone (b), [01 $\bar{1}$ ] zone (c), and [012] zone (d), which agree well with the experimental SAED (Figure 5) diffraction patterns.

is shown to be around 1.3 times the length of the molecule because of the bending of the bulky POSS groups and the interdigitated packing nature of the dimers (note that the length of a fully extended molecule without bending of the POSS groups is 3.910 nm). An important feature in this packing scheme is the longitudinal, transverse, and rotational offset. Similar rotational offsets of the PDI derivatives with ethyl and benzyl substituents have been reported before.<sup>51,52</sup> In this case, a series of complex offsets of the PDI planes is induced probably both by the electrostatic interactions and steric demands of the bulky POSS groups from the rigid 1,4-phenylene linkage. Starting from the perfect face-to-face parallel packing PDI dimers, a distortion by both the longitudinal and transverse offsets of the PDI planes was introduced. The longitudinal displacement of  $\sim 0.052$  nm and the transverse displacement of  $\sim 0.092$  nm, respectively, leads to a triclinic structure with  $\beta = 94.85^\circ$  and  $\gamma = 92.73^\circ$ . The rotational offsets are then introduced along the normal of PDI plane. Based on the unit cell dimensions determined using the experimental observations, there are six pairs of PDI dimers in one unit cell. To maintain the long-range order of the layer structure along the  $a$ -axis and minimize this long spacing period with the translational symmetry, the best rotational angle of the PDI plane relative to each other was found to be  $3^\circ$ . Their torsion angles are thus assigned to be  $-1.5^\circ$ ,  $-4.5^\circ$ ,  $-1.5^\circ$ ,  $+1.5^\circ$ ,  $+4.5^\circ$ , and  $+1.5^\circ$ , respectively, which would fulfill the  $a$ -axis dimension of 6.577 nm. As a result, a large spacing along the  $a$ -axis in this triclinic lattice can be found in this molecular packing scheme.

The constructed molecular packing scheme can then serve as a model system to simulate ED patterns along different zones and compare with the experimental SAED results. Figure 10 shows a series of simulated ED patterns from different zones generated by the crystal packing scheme of Figure 8. It is evident that the simulated ED patterns agree well with our experimental results. Specifically, the rotational offsets of the PDI cores are not significant enough to disrupt the ordered layer packing along the  $a$ -axis in one unit cell. This result of the strong (600) diffraction intensity in our simulated data (Figure 10) fits well with both our TEM and 2D WAXD results. In addition, the

observed  $c$ -axis with a dimension of 1.107 nm in our 2D WAXD and TEM results is attributed to the edge-edge organization of molecule **3** as shown in Figure 8.

The reason for **3**'s tendency toward elongated self-assembly is evident based on the crystal packing scheme shown in Figure 9. The long axis of the nanobelt is along the  $c^*$ -axis, and thus, the growing direction is the [001], normal to the  $ab$ -plane. The other two growth directions along the  $a^*$ - and  $b^*$ -axes are close to the growth fronts of the  $bc$ -plane and the  $ac$ -plane because the crystalline lattice is not that different from an orthorhombic lattice. The shape persistence of the packing motif, the dimer, has a well-defined, anisotropic, parallelepiped shape that possesses three distinctly different cross-sectional areas. Its attachment to the  $ab$ -plane from the side with the largest cross section thus most effectively decreases the surface free energy during the crystal growth and, therefore, reduces the barrier for crystal nucleus formation. The slower growth along the  $a^*$ -axis (the  $bc$ -plane) is from the side of the dimer with the second largest cross section. It also requires interdigitation along the  $a^*$ -axis dimers. This is energetically unfavorable by a direct contact between nonpolar POSS nanoparticle and the PDI plane. The slowest growth along the  $b^*$ -axis (the  $ac$ -plane) can be explained by the difficulty of the stiff dimer to attach on a flat surface in an upright conformation from the side with the smallest cross section and the weak head-to-head interaction between these shape-persistent molecules. The nucleation barrier is expected to be the highest in this case. Therefore, the formation mechanism of the nanobelt-shaped single crystals in this shape-persistent molecule is due to the difference of the nucleation barriers on the growth fronts of the  $ab$ -,  $ac$ -, and  $bc$ -planes, and thus, very anisotropic growth rates along these directions exist to construct this nanobelt-like supramolecular assembly. This analysis is based on crystallization in solution and the observed morphology with the elongated  $c$ -direction (growth of  $ab$ -plane).

## Conclusions

In summary, a shape-persistent, POSS-nanoparticle-tethered perylene diimide molecule has been designed and synthesized. The molecule can be self-assembled into crystalline nanobelts by slow evaporation from solutions in THF on various surfaces such as carbon-coated mica. The crystal structure and phase behavior of the material have been determined through a variety of experiment techniques. On the basis of our 2D WAXD results on the oriented crystal samples and SAED results on the nanobelts, a large triclinic unit cell of  $a = 6.577$  nm,  $b = 5.213$  nm,  $c = 1.107$  nm,  $\alpha = 93.26^\circ$ ,  $\beta = 94.85^\circ$ , and  $\gamma = 92.73^\circ$ , is deduced with a supramolecular dimer motif consisting of 12 molecules in one unit cell. On the basis of the experimental results of concentration-dependent ultraviolet/visible absorption spectra, fluorescence spectra, and tandem mass spectroscopy with traveling wave ion mobility separation, the molecules first pack into dimers to maximize their  $\pi$ - $\pi$  interactions and the dimers then pack into crystal lattices. This complex structure with the large  $a$ -axis dimension can be attributed to the longitudinal, transverse, and slight rotational offsets of the PDIs in each of the dimers and the interdigitation among the neighboring dimers. The molecular packing scheme of the crystal is simulated utilizing the crystallographic Cerius<sup>2</sup> software package. The simulated diffraction data agree well with the diffraction results observed in the WAXD and SAED experiments. The packing scheme can account for the highly anisotropic crystal growth along different axis and the resultant nanobelt formation. Although **3**'s electronic properties such as charge mobility might



be compromised due to the interruption of the  $\pi$ - $\pi$  stacking, the current work has more implications in elucidating the effect of different factors on self-assembly such as shape and conformation rigidity and in improving our understanding in solid-state packing of these materials which can guide the design of functional systems in the future. Further work on the electronic properties of **3** and its derivatives are ongoing in our group.

**Acknowledgment.** The authors thank Dr. Bernard Lotz and Dr. Bojie Wang for helpful and insightful discussions. This work was supported by the National Science Foundation (DMR-0906898, CHE-0517909, CHE-0833087, and DMR-0821313). X.R. acknowledges the China Scholarship Council for support, and W.-B.Z. acknowledges the Lubrizol Corp. for a fellowship.

**Supporting Information Available:**  $^1\text{H}$  NMR,  $^{13}\text{C}$  NMR spectra of **3** and the table of crystallographic parameters. This material is available free of charge via the Internet at <http://pubs.acs.org>.

## References and Notes

- (1) Klauk, H. *Organic Electronics: Materials, manufacturing and applications*; Wiley-VCH: Weinheim, Germany, 2006.
- (2) Hoeben, F. J. M.; Jonkheijm, P.; Meijer, E. W.; Schenning, A. P. H. J. *Chem. Rev.* **2005**, *105*, 1491–1546.
- (3) Zang, L.; Che, Y. K.; Moore, J. S. *Acc. Chem. Res.* **2008**, *41*, 1596–1608.
- (4) Wu, J. S.; Pisula, W.; Mullen, K. *Chem. Rev.* **2007**, *107*, 718–747.
- (5) Treier, M.; Nguyen, M. T.; Richardson, N. V.; Pignedoli, C.; Passerone, D.; Fasel, R. *Nano Lett.* **2009**, *9*, 126–131.
- (6) Graja, A. *Low-dimensional organic conductors*; World Scientific: Singapore, 1992.
- (7) Zhao, Y. S.; Fu, H. B.; Peng, A. D.; Ma, Y.; Xiao, D. B.; Yao, J. N. *Adv. Mater.* **2008**, *20*, 2859–2876.
- (8) Chen, Z. J.; Lohr, A.; Saha-Moller, C. R.; Wurthner, F. *Chem. Soc. Rev.* **2009**, *38*, 564–584.
- (9) Laschat, S.; Baro, A.; Steinke, N.; Giesselmann, F.; Hagele, C.; Scalia, G.; Judele, R.; Kapatsina, E.; Sauer, S.; Schreivogel, A.; Tosoni, M. *Angew. Chem., Int. Ed.* **2007**, *46*, 4832–4887.
- (10) Mas-Torrent, M.; Durkut, M.; Hadley, P.; Ribas, X.; Rovira, C. *J. Am. Chem. Soc.* **2004**, *126*, 984–985.
- (11) Tang, C. W.; Van Slyke, S. A. *Appl. Phys. Lett.* **1987**, *51*, 913–915.
- (12) Kafafi, Z. H. *Organic electroluminescence*; CRC Press, Taylor & Francis: Boca Raton, FL, 2005.
- (13) Tang, C. W. *Appl. Phys. Lett.* **1986**, *48*, 183–185.
- (14) Dodabalapur, A.; Torsi, L.; Katz, H. E. *Science* **1995**, *268*, 270–271.
- (15) Newman, C. R.; Frisbie, C. D.; da Silva, D. A.; Bredas, J. L.; Ewbank, P. C.; Mann, K. R. *Chem. Mater.* **2004**, *16*, 4436–4451.
- (16) Bao, Z.; Locklin, J. J. *Organic field-effect transistors*; CRC Press: Boca Raton, FL, 2007.
- (17) Che, Y.; Yang, X. M.; Zang, L. *Chem. Commun.* **2008**, 1413–1415.
- (18) Schmidt-Mende, L.; Fechtenkotter, A.; Mullen, K.; Moons, E.; Friend, R. H.; MacKenzie, J. D. *Science* **2001**, *293*, 1119–1122.
- (19) Struijk, C. W.; Sieval, A. B.; Dakhurst, J. E. J.; Van Dijk, M.; Kimkes, P.; Koehorst, R. B. M.; Donker, H.; Schaafsma, T. J.; Picken, S. J.; van de Craats, A. M.; Warman, J. M.; Zuilhof, H.; Sudholter, E. J. R. *J. Am. Chem. Soc.* **2000**, *122*, 11057–11066.
- (20) Cui, L.; Collet, J. P.; Xu, G. Q.; Zhu, L. *Chem. Mater.* **2006**, *18*, 3503–3512.
- (21) Xu, Y. J.; Leng, S. W.; Xue, C. M.; Sun, R. K.; Pan, J.; Ford, J.; Jin, S. *Angew. Chem., Int. Ed.* **2007**, *46*, 3896–3899.
- (22) Würthner, F. *Chem. Commun.* **2004**, 1564–1579.
- (23) Katz, H. E.; Lovinger, A. J.; Johnson, J.; Kloc, C.; Siegrist, T.; Li, W.; Y.-Y., L.; Dodabalapur, A. *Nature* **2000**, *404*, 478–481.
- (24) Shirota, Y.; Kageyama, H. *Chem. Rev.* **2007**, *107*, 953–1010.
- (25) Everett, T. A.; Twite, A. A.; Xie, A. F.; Battina, S. K.; Hua, D. H.; Higgins, D. A. *Chem. Mater.* **2006**, *18*, 5937–5943.
- (26) Liu, S. G.; Sui, G. D.; Cormier, R. A.; Leblanc, R. M.; Gregg, B. A. *J. Phys. Chem. B* **2002**, *106*, 1307–1315.
- (27) Baram, J.; Shirman, E.; Ben-Shitrit, N.; Ustinov, A.; Weissman, H.; Pinkas, I.; Wolf, S. G.; Rybtchinski, B. *J. Am. Chem. Soc.* **2008**, *130*, 14966–14967.
- (28) Che, Y. K.; Datar, A.; Balakrishnan, K.; Zang, L. *J. Am. Chem. Soc.* **2007**, *129*, 7234–7235.
- (29) Balakrishnan, K.; Datar, A.; Naddo, T.; Huang, J. L.; Oitker, R.; Yen, M.; Zhao, J. C.; Zang, L. *J. Am. Chem. Soc.* **2006**, *128*, 7390–7398.
- (30) Ghosh, S.; Li, X. Q.; Stepanenko, V.; Würthner, F. *Chem.-Eur. J.* **2008**, *14*, 11343–11357.
- (31) Leng, S. W.; Wex, B.; Chan, L. H.; Graham, M. J.; Jin, S.; Jing, A. J.; Jeong, K. U.; Van Horn, R. M.; Sun, B.; Zhu, M. F.; Kaafarani, B. R.; Cheng, S. Z. D. *J. Phys. Chem. B* **2009**, *113*, 5403–5411.
- (32) Leng, S. W.; Chan, L. H.; Jing, J.; Hu, J.; Moustafa, R. M.; Van Horn, R. M.; Graham, M. J.; Sun, B.; Zhu, M. F.; Jeong, K. U.; Kaafarani, B. R.; Zhang, W. B.; Harris, F. W.; Cheng, S. Z. D. *Soft Matter* **2010**, *6*, 100–112.
- (33) Li, G. Z.; Wang, L. C.; Ni, H. L.; Pittman, C. U. *J. Inorg. Org. Polym.* **2001**, *11*, 123–154.
- (34) Wu, J.; Mather, P. T. *Polym. Rev.* **2009**, *49*, 25–63.
- (35) Xiao, S.; Nguyen, M.; Gong, X.; Cao, Y.; Wu, H. B.; Moses, D.; Heeger, A. J. *Adv. Funct. Mater.* **2003**, *13*, 25–29.
- (36) Moore, J. S. *Acc. Chem. Res.* **1997**, *30*, 402–413.
- (37) Wegner, G. *Macro. Chem. Phys.* **2003**, *204*, 347–357.
- (38) Zhao, D. H.; Moore, J. S. *Chem. Commun.* **2003**, 807–818.
- (39) Balakrishnan, K.; Datar, A.; Zhang, W.; Yang, X. M.; Naddo, T.; Huang, J. L.; Zuo, J. M.; Yen, M.; Moore, J. S.; Zang, L. *J. Am. Chem. Soc.* **2006**, *128*, 6576–6577.
- (40) Langhals, H. *Heterocycles* **1995**, *40*, 477–500.
- (41) Chan, Y. T.; Li, X. P.; Soler, M.; Wang, J. L.; Wesdemiotis, C.; Newkome, G. R. *J. Am. Chem. Soc.* **2009**, *131*, 16395–16397.
- (42) Wicklein, A.; Ghosh, S.; Sommer, M.; Würthner, F.; Thelakkat, M. *ACS Nano* **2009**, *3*, 1107–1114.
- (43) Balakrishnan, K.; Datar, A.; Oitker, R.; Chen, H.; Zuo, J. M.; Zang, L. *J. Am. Chem. Soc.* **2005**, *127*, 10496–10497.
- (44) Eashoo, M.; Wu, Z. Q.; Zhang, A. Q.; Shen, D. X.; Tse, C.; Harris, F. W.; Cheng, S. Z. D.; Gardner, K. H.; Hsiao, B. S. *Macro. Chem. Phys.* **1994**, *195*, 2207–2225.
- (45) Jing, A. J.; Taikun, O.; Li, C. Y.; Harris, F. W.; Cheng, S. Z. D. *Polymer* **2002**, *43*, 3431–3440.
- (46) Ge, J. J.; Zhang, A. Q.; McCreight, K. W.; Ho, R. M.; Wang, S. Y.; Jin, X. M.; Harris, F. W.; Cheng, S. Z. D. *Macromolecules* **1997**, *30*, 6498–6506.
- (47) Ruan, J. J.; Ge, J. J.; Zhang, A. Q.; Shi, J.; Wang, S. Y.; Harris, F. W.; Cheng, S. Z. D. *Macromolecules* **2002**, *35*, 736–745.
- (48) Bohrer, B. C.; Mererblom, S. I.; Koeniger, S. L.; Hilderbrand, A. E.; Clemmer, D. E. *Annu. Rev. Anal. Chem.* **2008**, *1*, 293–327.
- (49) Clemmer, D. E.; Jarrold, M. F. *J. Mass Spectrom.* **1997**, *32*, 577–592.
- (50) Kanu, A. B.; Dwivedi, P.; Tam, M.; Matz, L.; Hill, H. H. J. *J. Mass Spectrom.* **2008**, *43*, 1–22.
- (51) Graser, F.; Hadicke, E. *Liebigs Ann. Chem.* **1984**, 483–494.
- (52) Zugenmaier, P.; Duff, J.; Bluhm, T. L. *Cryst. Res. Technol.* **2000**, *35*, 1095–1115.

JP100126U